The Cyprus Journal of Science and Technology Vol. 5, No. 2, 2006

NOVEL INTELLIGENT SENSOR FOR RECONFIGURABLE SPACE PHYSICS SYSTEMS

G. Dekoulis[1], F. Honary[2]

[1] *Department of Computer Engineering, Frederick Research Centre,*
Nicosia, Cyprus
[2] *Space Plasma Environment and Radio Science Group, Department of Communication*
Systems, Lancaster University, UK

Abstract. This paper describes the design of a novel flexible and intelligent sensor for remote earth sensing space applications. The development of such a sensor is strongly related to the recent technical advancements of MEMS sensors. The design methodology is focused on supporting subsequent reconfigurable and adaptive ground-based space physics systems, installation on pico-satellites and micro-spacecrafts, and micro-sensors.

Keywords: Space physics, reconfigurable, intelligent sensors.

1. INTRODUCTION

Intelligent sensors scientifically describe sensors that focus on functionality rather than calculating the measurand. The level of sophistication incorporated by sensors considered to be intelligent ranges from incorporating an operational amplifier amplifying the output signals driving the next instrumentation stage of a pico-satellite to progressive data modelling routines for monitoring the earth's magnetic field in a micro-spacecraft [1]. Current research investigates sensor and micro-sensor design as well as experimenting with advanced accompanying digital signal processing algorithms [2]. An intelligent sensor approach can enhance the active sensor's management system. The higher logical-level of the sensor's organisational system is progressively being improved by further guaranteeing the reliability of the acquired sensor's data. On-board condition monitoring and fault detection hardware techniques can satisfy the sensor's redundancy for implementing robust measurements. Advanced data-based modelling techniques model non-linear and time-variant sensor systems, avoiding the limitations of linear physical sensor models, and allowing the sensor's reconfiguration to correct for sensor ageing and drift mechanisms [3].

Intelligent sensors are in general autonomous, adaptive to changes in their environment and self-adjusting to drift and bias effects caused by mechanisms such as ageing of the sensing element. The principal characteristic of such n intelligent sensor is that it communicates reliably with self-validation signals or features to the higher level supervision systems, for purposes such as information fusion, tracking, estimation and direction finding of the earth's magnetic field [4]. Poor sensory data should be identified by the sensor, and GPS tagged for quality problems, together with estimates of the likely cause to enable correction during the sensor's reconfiguration.

---

* Corresponding author. *Tel.: +357 22 431355, Fax: +357 22 438234*
E-mail Address: eng.gd@fit.ac.cy

Intelligent fluxgate sensors are commonly used to measure the Earth's magnetic field. Modern research is based on sensor miniaturisation and the implementation of enriched materials. Fluxgates are non-semiconductor sensors already using micro-technologies. Latest technology micromachining processes are used in designing micro-coils and micro-relays [5]. Wires and tapes are amorphous materials applied to sensors [6].

Fluxgate sensors measure the 0 Hz or low frequency ac magnetic field vector in the range of 1^{-10} to 10^{-4} T. An ac excitation field of frequency f through the excitation coil drives the soft magnetic core to saturation, as illustrated in Fig. 1. The core permeability changes with 2f frequency and the dc flux $\Phi(t)$ is modulated. Flux is derived from the external dc magnetic field Bo. An induced voltage proportional to Bo at the second and higher even harmonics of the excitation frequency is measured at the measuring coil of N turns [7].

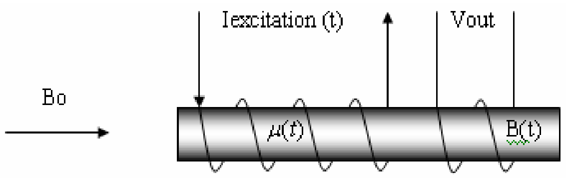

Fig. 1. The Fluxgate Principle using a Parallel Type Sensor.

The work on fluxgate sensors started from the late 1920s and the first patent was in 1931 [8]. Fluxgate sensors have been used on the Moon and in deep space [9]. They are solid-state devices with no moving parts and can work under different temperatures. Commercial sensors have roughly resolution and absolute precision of 100 pT and 10 nT, respectively. They operate between several Hz up to kHz. A drift of 0.1 nT/1° C and a sensitivity coefficient up to 1 ppm/° C in certain cases prove their stability with temperature. A typical linearity is 30 ppm.

There are two categories of fluxgate sensors. The first category is the orthogonal type sensors. As the name implies, the excitation field is perpendicular to the sensitive axis of the sensor. The pioneer of this type is Alldredge [10] and the sensor has a core of a ferromagnetic wire or a tube. A current excites the core in the first type, however the disadvantage is that at the core centre the excitation field is zero, which affects the sensor remanence. The tube type is excited by one wire in the tube [11]. A helically wounded tape on a tube forms an orthogonal-parallel sensor [12].

In orthogonal type sensors the excitation field is perpendicular to the sensitive axis of the sensor. The sensor has a core of a ferromagnetic wire or a tube. A current excites the core in the first type, however the disadvantage is that at the core centre the excitation field is zero, affecting the sensor remanence. The tube type is excited by one wire in the tube [11]. A helically wounded tape on a tube forms an orthogonal-parallel sensor [12].

However, parallel type sensors have better performance and they are more suitable for a low-noise fluxgate. For a low-noise precision fluxgate the ring-core parallel type or double-rod sensors should be investigated. Single core sensors are used for undemanding applications [13], due to the induced transformer effect and the odd harmonics at the output. This can be solved using a double-core sensor. The two parallel excitation cores are excited in opposite directions in order to nullify the mutual inductance between the sensing and excitation coils [14]. Two serially connected excitation coils permit flexible matching and sensor balancing by moving the excitation coils with respect to their sensing coils [15]. Open-ended rods present increased sensitivity, directivity and resistance to orthogonal fields, but have a higher noise figure, vulnerability to perming effects and temperature offset drifts, difficulty in saturation and high power consumption.

The choice left is between the ring-core and race-track sensors. Race track sensors have lower demagnetisation factor, higher directional sensitivity, less sensitivity to orthogonal fields (interference) [16]. Race-track sensors exhibit large unbalanced spurious signals and problems from higher tape pressure in the corners. Ring-core sensors have an anuloid excitation coil and a solenoid-sensing coil. Although they have low sensitivity due to the demagnetisation, ring-core designs have many advantages and produce low-noise sensors. Rotating the core with respect to the sensing coil permits precision balancing of the core symmetry. Ring-core sensors exhibit uniform distribution of any mechanical stress. The increased noise associated with open-ended rods is absent. Tape ends are an insignificant source of noise. Sensitivity is proportional to the sensor diameter. For a given diameter, a trial-by-error procedure was followed to determine the optimum for the other dimensions.

2. INTELLIGENT SENSOR DESIGN STUDY RESULTS

Several intelligent sensors of the race-track and ring-core types have been designed and simulated using the Finite Integration Theory (FIT) method. FIT is strongly associated with the Finite Difference Time Domain (FDTD) method. However, FIT contains in the time domain both static and the frequency domain. These simulations can obtain the complete sensor response.

The basic simulation model of Fig. 2 consists of an excitation coil of 240 turns and a sensor coil of 50 turns. The aim is to create an optimised sensor that saturates at a current much smaller (<100mA) than the values quoted in the papers reviewed (≈ 1A), as in [17-18], in order to significantly reduce the power consumption by a factor of sixteen. Low power consumption has only been seen on MEMS sensors [19], after extensive optimisation of the structure, usually by following a trial-by-error procedure. This initial design is a combination of a race-track of 8 layers etched from a sheet of amorphous magnetic material [20] embedded in the shape of a standard MEMS square fluxgate sensor [21]. In this way, the new design is inheriting the advantages of both technologies.

(a) *(b)*

Fig. 2. (a) xy, (b) yz, Projections of the Basic Race-Track Intelligent Sensor.

At a first glance, the selection of the square top frame is a poor choice in terms of electromagnetic performance and requires an extensive optimisation procedure. Practically, a rectangle with an aspect ratio of length (x) / width (y) ≈ 3 and the sensor coiled around the middle of the two x branches is the natural choice for single-axis measurements. The y-axis of Fig. 2 could also accommodate a second sensor coil measuring the y-dimension.

The excitation coil has been modelled as 8 coils connected in series. Each coil has 30 turns. Different soft [22-23] and hard magnetic materials [22-24] have been considered for modelling the core and a list of suitable soft magnetic materials is in Table 1. However, hard magnetic materials exhibit a wide B (H) curve and were at once eliminated from the selection process.

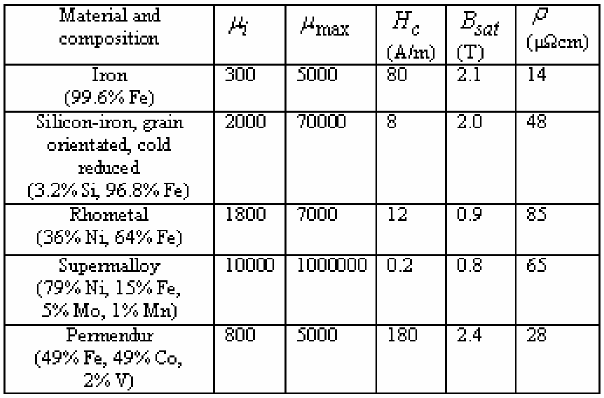

Material and composition	μ_i	μ_{max}	H_c (A/m)	B_{sat} (T)	ρ (μΩcm)
Iron (99.6% Fe)	300	5000	80	2.1	14
Silicon-iron, grain orientated, cold reduced (3.2% Si, 96.8% Fe)	2000	70000	8	2.0	48
Rhometal (36% Ni, 64% Fe)	1800	7000	12	0.9	85
Supermalloy (79% Ni, 15% Fe, 5% Mo, 1% Mn)	10000	1000000	0.2	0.8	65
Permendur (49% Fe, 49% Co, 2% V)	800	5000	180	2.4	28

Table 1. Soft Magnetic Alloys.

The appropriate material would have a high as possible maximum permeability μ and a low as possible saturation flux density Bsat. The supermalloy material is chosen for this study. The corresponding B (H) characteristic curve is in Fig. 3. Supermalloy has a steep slope in the easy magnetisation region and a reasonable flat slope in the hard magnetisation region towards magnetic saturation.

The sensor's response is obtained by applying an external field of 1T in the x direction, as in Fig. 4. The sensor can be rotated around its axis to obtain measurements of its directionality. During 3-dimensional transient analysis, a 5 KHz square wave of +/- 250 mA was injected to the excitation coil by a single current source. The sensor's response is found by the voltage at the sensor coil's output.

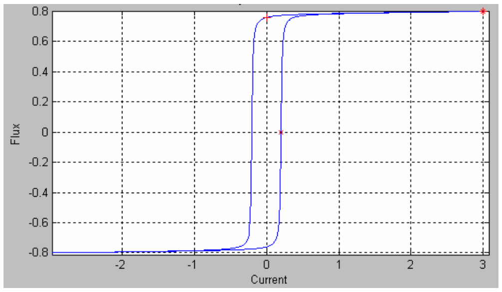

Fig. 3. Supermalloy Magnetisation B(H) Curve (T(A/m)).

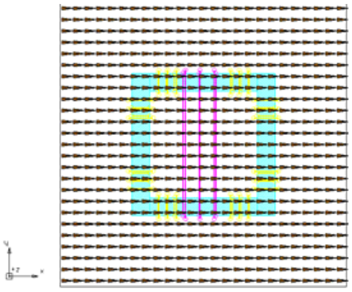

Fig. 4. X-Axis External Vector Field (1 T).

At instance 0, when no current is applied to the excitation coil the structure absorbs the incoming wave, as in Fig. 5, using an arrow and a contour diagram.

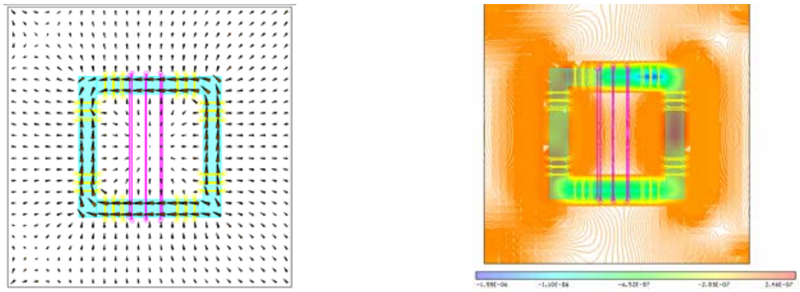

(a) *(b)*

Fig. 5. (a) Arrow (b) Contour Diagrams of B (Iexc = 0).

The results when the excitation current reaches its maximum value are presented in Fig. 6 (a) and (b), using an arrow and a contour diagram. At saturation the low-y and high-y branches of the core resume the Bsat value of 0.8 T. The magnetic flux density due to the external field outside the core is 0, since all magnetic lines are repressed. The permeability distribution at saturation is presented in Fig. 7 (a).

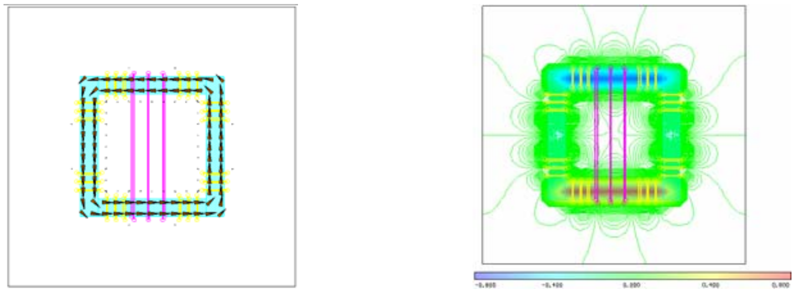
(a) *(b)*

Fig. 6. (a) Arrow and (b) Contour Diagrams of B at Magnetic Saturation.

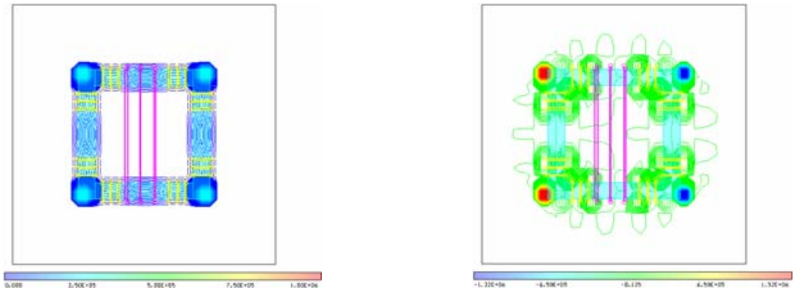
(a) *(b)*

Fig. 7. (a) Permeability Distribution at Magnetic Saturation, (b) Maxwell Stress and Lorentz Force Distribution.

The force F for the xyz coordinate system (Fx, Fy and Fz) and torque M on the z-axis (Mz) results are tabulated for the different materials in Table 2. The distribution of the force and torque within the 3-dimensional sensor is plotted in Fig. 7 (b). The force is calculated using the Maxwell's stress tensor and Lorentz force for the excitation coil and sensor's winding. The Maxwell's stress tensor calculates the surface integral of the material area where the force under study is applied. It requires knowledge of the flux density and field strength allocated on the grid or dual grid if high accuracy results are needed. The hot red and blue areas near the corners of the core represent the areas not taken into account in the calculation of the integral. However, the validity of the results is not affected and it is overcome for circular/torus cores.

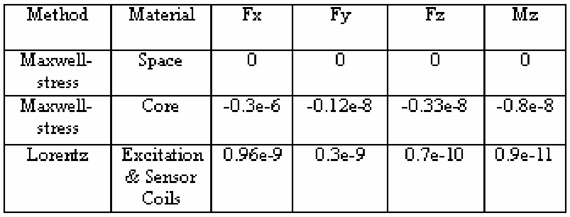

Method	Material	Fx	Fy	Fz	Mz
Maxwell-stress	Space	0	0	0	0
Maxwell-stress	Core	-0.3e-6	-0.12e-8	-0.33e-8	-0.8e-8
Lorentz	Excitation & Sensor Coils	0.96e-9	0.3e-9	0.7e-10	0.9e-11

Table 2. Maxwell Stress and Lorentz Force Results.

During the transient response analysis the electric field strength, magnetic flux density, eddy currents and relative permeability have all been monitored. Based on these measurements the voltage or electromotive force (EMF) can be calculated using the Faraday's law [25], expressed by eq. (1):

$$V = \oint EdL = -\iint \frac{\partial B}{\partial t} ds \qquad (1)$$

where, $\oint EdL$ is the line integral around the sensor coil,

$\iint \frac{\partial B}{\partial t} ds$ is the surface integral of $\frac{\partial B}{\partial t}$ over the sensor coil.

The raw voltage output depends on all the parameters taken into account in the above simulations and it also should contain harmonics of the excitation field. A monotonic excitation field can be expressed by eq. (2):

$$H = H_{\max} \sin(\omega t) \qquad (2)$$

The symmetrical B(H) characteristic curve used to model the nonlinearity of the supermalloy core is by definition a third order polynomial, which can be written as:

$$B(H) = a_1 H - a_3 H^3 \qquad (3)$$

From the arrow plots of Fig. 5 (a) and Fig. 6 (a) it is obvious that no matter whether the core is just at the zero crossing of the initial magnetisation curve or at the end of the hard magnetisation region towards saturation, respectively, there subsists an internal strictly oriented circulating field. In the former figure due to the external field only, while in the latter due to the excitation field only. During normal operation within the linear magnetisation region this field is a concoction of both and seizes the form of eq. (4):

$$H_{core} = H_{space} + H \qquad (4)$$

Stepping into Faraday's law:

$$V = -NA\frac{\partial B}{\partial t} \tag{5}$$

Normalising the output voltage and solving:

$$\begin{aligned} V_n &= -\frac{V}{NA} = \\ &= B_{\max}\omega(a_1 H_{\max} - 3a_3 H_{\max} H_{space}^2 - \frac{3}{4}a_3 H_{\max}^3)\cos(\omega t) \\ &+ 3B_{\max}\omega a_3 H_{space} H_{\max}^2 \sin(2\omega t) \\ &+ \frac{3}{4} B_{\max}\omega a_3 H_{\max}^2 \cos(3\omega t) \end{aligned} \tag{6}$$

The product containing the sin (2ωt) factor is the second harmonic output:

$$V_2 = 3B_{\max}\omega a_3 H_{space} H_{\max}^2 \sin(2\omega t) = \psi \sin(2\omega t) \tag{7}$$

where, $\psi = 3B_{\max}\omega a_3 H_{space} H_{\max}^2$

The output voltage is a function of the external field applied, excitation field, excitation frequency, core size and the characteristic curve of the chosen material. In parallel type cores the second harmonic is derived using magnetic filtering, which involves matching two identical linear probes measuring the field difference between two points. This matching is avoided using a structure such as the one presented already.

Additionally, in parallel type sensors excellent bandpass filters are needed to distinguish the 2nd from the 1st and 3rd harmonics. The advantage of using a structure such as in Fig. 2 is that all odd harmonics are nullified without using magnetic filtering and just a low pass filter near the 3rd (15 KHz) or 4th (20 KHz) harmonic is required to extract the 2nd harmonic.

A Matlab Simulink model is processing the sensor's output. A 15th order FIR butterworth low pass filter with cut-off frequency at the 3rd harmonic (15 KHz) is implemented for a sampling frequency of 100 KHz, while its frequency response is plotted in Fig. 8.

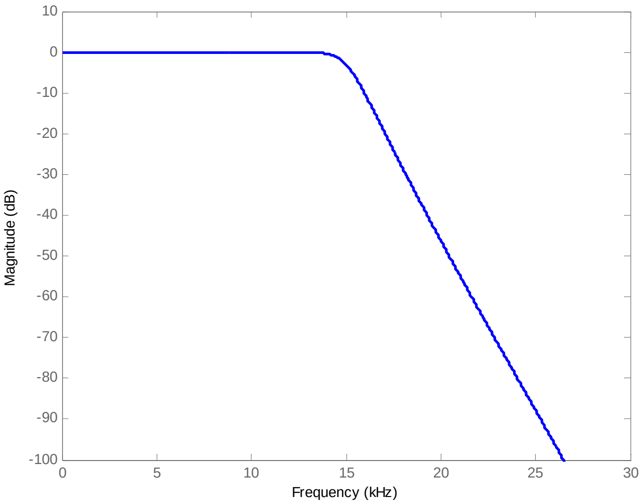

Fig. 8. FIR LPF Filter Frequency Response.

The sensor’s filtered output for a 150 uT external magnetic field is in Fig. 9. The peak-to-peak voltage is measured to be 29.6 mV.

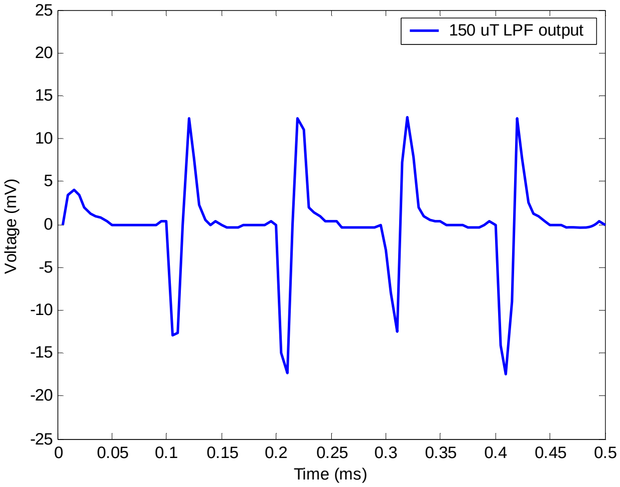

Fig. 9. Intelligent Sensor’s Output Response for B = 150 uT.

The above simulations have been repeated for a set of different external field values between 0 and 300 uT and the values of most importance are in Fig. 10.

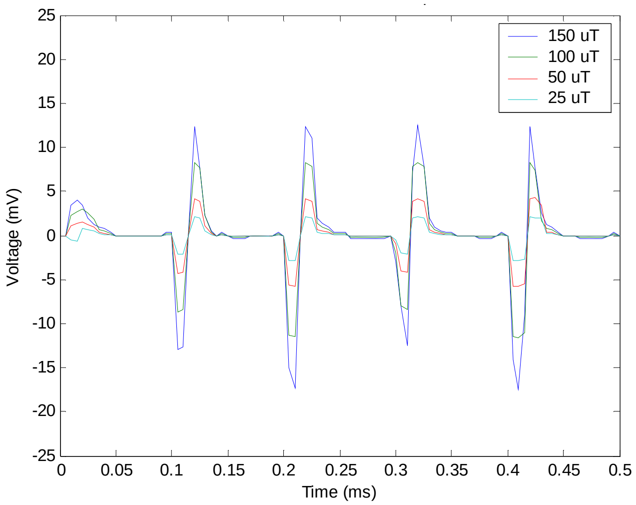

Fig. 10. Intelligent Sensor's Output Response for B = 25, 50, 100 and 150 uT.

The Vpp results of all the simulations are plotted in Fig. 11 to portray the sensor's sensitivity. The measured sensitivity is 189 uV/nT.

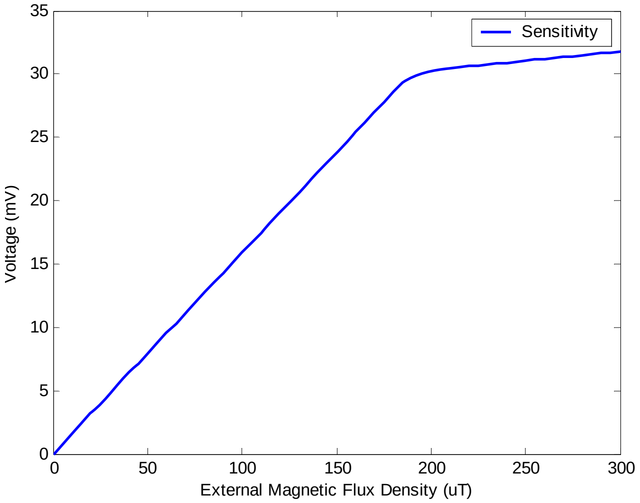

Fig. 11. Intelligent Sensor's Sensitivity Diagram.

3. INTELLIGENT SENSOR'S OPTIMISATION TECHNIQUE RESULTS

At the zero-crossing of the initial magnetisation curve the external magnetic field is attracted by the core, as in Fig. 12 (a) and flows through the core due to its weak reluctance, as in Fig. 12 (b). The opposite situation exists when the core is at saturation. In Fig. 12 (b), the external magnetic field is entering the structure from branch 1, is split between branches 2 and 3 and exits the structure through branch 4.

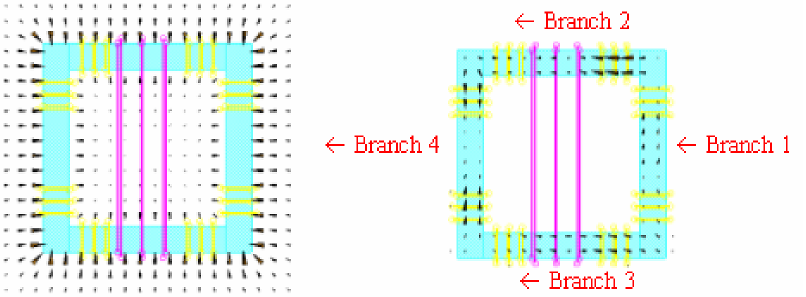

(a) *(b)*

Fig.12. (a) External Field (b) External Field Flow Through the Core at Premagnetisation.

The opposition to magnetic flux in any branch of the core is called reluctance $\Re$ [26]:

$$\Re = \frac{l}{A\mu_o\mu_r} \qquad (8)$$

where $\Re$ is the reluctance (A-turns/Wb), l the length (m), μ_o the permeability of free space, μ_r the relative permeability (H/m) and A is the cross-sectional area of the magnetic circuit (m^2).

Consider the structure of Fig. 13 (a) and its equivalent magnetic model in Fig. 13 (b). Reluctance in magnetism is the represented by resistance in electrism. The flux through R1, R4-6 and R9-10 is the same since they are in series. The flux through R2 and R3 equals to:

$$\Phi_2 = \Phi_3 \frac{R_3}{R_1 + R_2} \quad \text{and} \quad \Phi_3 = \Phi_2 \frac{R_2}{R_1 + R_2} \qquad (9)$$

$$\frac{\Phi_3}{\Phi_2} = \frac{R_2}{R_3} = \mu_r \frac{A_3}{A_2} = 10^6 \Rightarrow \Phi_3 >> \Phi_2 \qquad (10)$$

The relative permeability is the maximum permeability in electromagnetics, 10^6, while the area ratio equals to 1. Therefore, the fringing flux through the air gap is negligible.

$$\Phi_1 \equiv \Phi_3 \equiv \Phi_4 \Rightarrow B_1 A_1 = B_3 A_3 = B_4 A_4 \qquad (11)$$

For $A_1 / A_3 = P$,

$$B_3 = P B_1 \qquad (12)$$

Therefore, the magnetic flux density through R3 and R7 is P times higher than the flux flowing through the rest of the magnetic circuit.

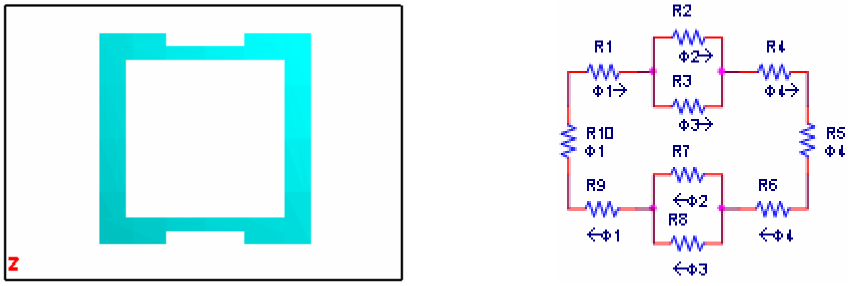

(a) *(b)*

Fig. 13. (a) Modified Core (b) Flux Flow Through the Modified Core.

From equations (13) and (14) [26] an expression is obtained relating B and the excitation current:

$$L = \frac{N\Phi}{I_{exc}} \Rightarrow \Phi = \frac{I_{exc} L}{N} \qquad (13)$$

$$B = \frac{\Phi}{A} \Rightarrow \Phi = BA \qquad (14)$$

$$BA = \frac{IL}{N} \Rightarrow B = I_{exc} \frac{L}{AN} \Rightarrow B \propto I_{exc} \quad (15)$$

From eq. (12) and (15) a solid relationship between the saturation currents is obtained:

$$I_{sat3} = \frac{I_{sat1}}{P} = \frac{I_{sat1}}{4} \approx 60mA \quad (16)$$

It has been shown that the field flowing through the structure is not the same as the field applied to the material. The magnetisation effect creates free poles at the edges of the structure. These poles in turn create an opposing field to the one applied. This effect is called demagnetisation [27]. The field inside the core equals:

$$H_{core} = \frac{H_{ext}}{1 + N_d \mu_r} \qquad (17)$$

where, Hcore is the internal field, Hext is the external field, Nd is the demagnetisation factor and μr the relative permeability of the supermalloy. A ferromagnetic ellipsoid is the only shape, which has the same magnetisation and demagnetisation fields throughout its structure. Using Cartesian coordinates Nd is diagonalised and the corresponding demagnetising factors for the xyz coordinates are combined by eq. (18):

$$N_x + N_y + N_z = 1 \qquad (18)$$

For a sphere: $N_x = N_y = N_z = 1/3$ (19)

For the simulated sensor of the previous section:

$$N_z = 1, N_x = N_y = 0 \qquad (20)$$

For sensors of the parallel type core, assuming the rod is placed on the y-axis:

$$N_y = 0, N_x = N_z = 0.5 \qquad (21)$$

In general, Nd decreases as the length versus cross-sectional area A ratio increases. In order to find the optimum sensor design several cores have been simulated and the magnetic flux through the core has been measured using the newly calculated excitation current value given by eq. (16). Fig. 14 shows the results from the previously simulated supermalloy sensor at the x-direction, which saturates at 0.8 T for an excitation current of 250 mA.

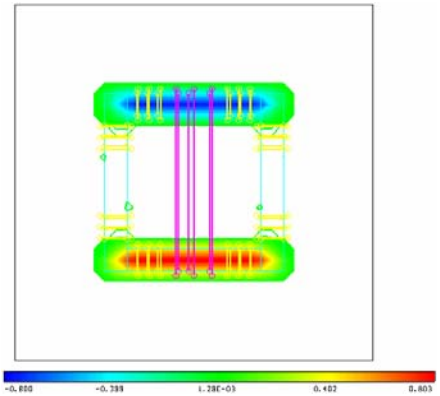

Fig. 14. Supermalloy Core at Saturation (B = 0.8 T, Iexc = 250 mA).

The excitation current has been reduced to 60 mA and the magnetic flux density in the x-direction is 0.3 T, as shown in Fig. 15. The core is no longer at saturation.

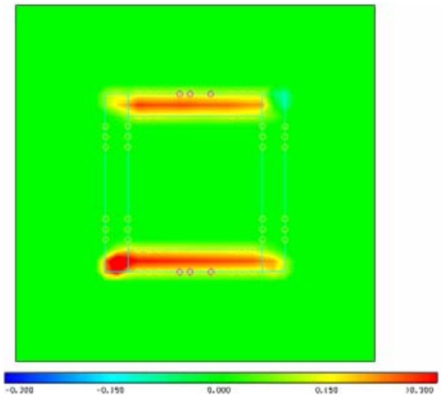

Fig.15. Magnetic Flux Density Distribution (B = 0.3 T, Iexc = 60 mA).

A link of 2.5 mm length (l) and 1 mm width (w) has been added corresponding to R3 of Fig. 13. For the same excitation current of 60 mA, B equals to 0.42 T, as shown in Fig. 16 (a). The core is not at saturation. The same link has been added in place of R2 of Fig. 13. As expected, the results of Fig. 16 (b) match the results of Fig. 16 (a).

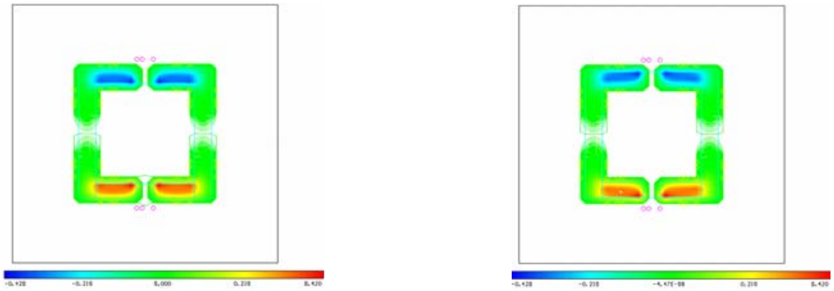

(a) (b)

Fig. 16. Magnetic Flux Density Distribution (B = 0.42 T, Iexc = 60 mA)
After Adding a Link in Place of (a) R3 (b) R2.

In Fig. 17 (a) the link's l is doubled to 5 mm and B is halved to 0.21 T. In Fig. 17 (b) the link is replaced by two cones facing each other with a total l of 3 mm and no space between them. B is measured to be 0.207 T. In Fig. 18 (a) a link of l = 5 mm and w = 1 mm between two cones of l=1.5 mm (total l = 8 mm) produces a B of 0.4 T. In Fig. 18 (b) the link's l = 2.5 mm and the cone's 1.5 mm producing a flux of 0.68 T. Fig. 19 shows the optimum structure for link's l = 2 mm, cone's l = 2 mm. The desired Bsat value is 0.8 T.

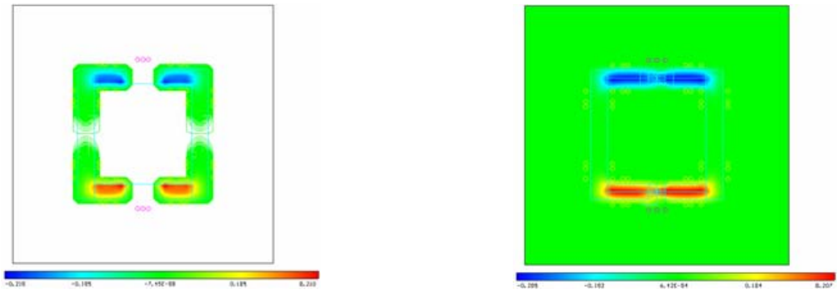

(a) (b)

Fig. 17. Magnetic Flux Density Distribution
(a) B = 0.21T, Iexc=60mA (b) B = 0.207T, Iexc=60mA.

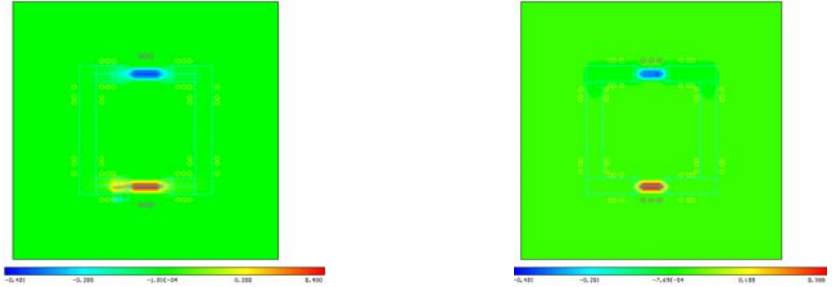

(a) (b)

Fig. 18. Magnetic Flux Density Distribution
(a) B = 0.4 T, Iexc=60 mA (b) B = 0.68 T, Iexc=60 mA.

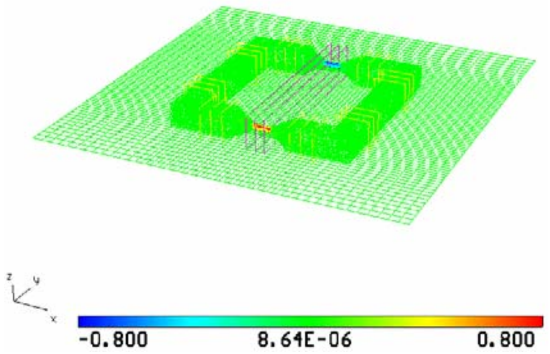

Fig. 19. Magnetic Flux Density Distribution
Bsat = 0.8 T, Iexc = 60 mA.

After a trial-by-error procedure the optimum core structure has been determined. The sensor is tested under the influence of a varying external field and the results for the bottom x-branch, of Fig. 19, are plotted in Fig. 20. The link exhibits a sensitivity of 197 uV/nT.

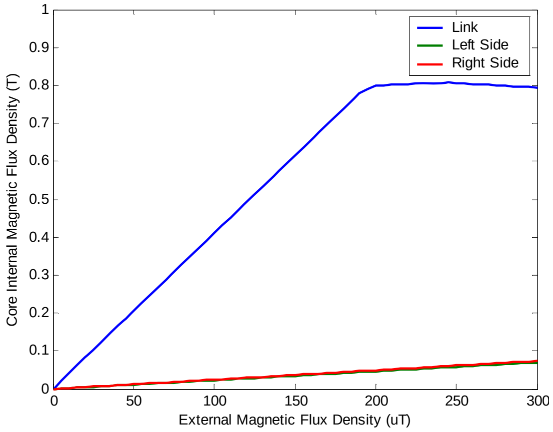

Fig. 20. Optimised Intelligent Sensor's Sensitivity Diagram for Bottom x-Branch.

The B field at 25, 50 and 100 uT is plotted. Vpp is measured to be 19.45 mV for an external B of 100 uT.

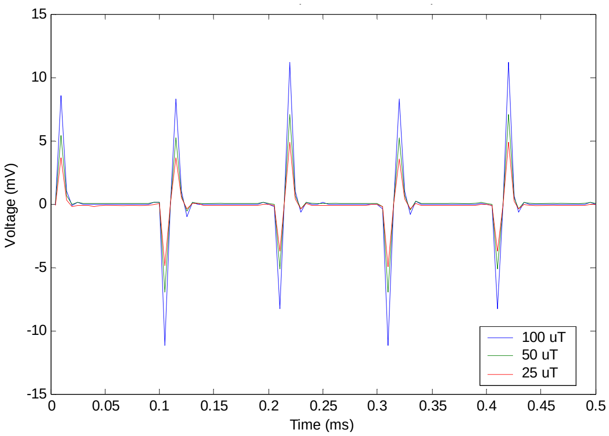

Fig.21. Intelligent Sensor's Output Response for B = 25, 50 and 100 uT.

The sensor exhibits a sensitivity of 151 uV/nT, as shown in Fig. 22. The output voltage response for external fields of 250 and 300 uT is in Fig. 23. The core is already saturated in the middle portion.

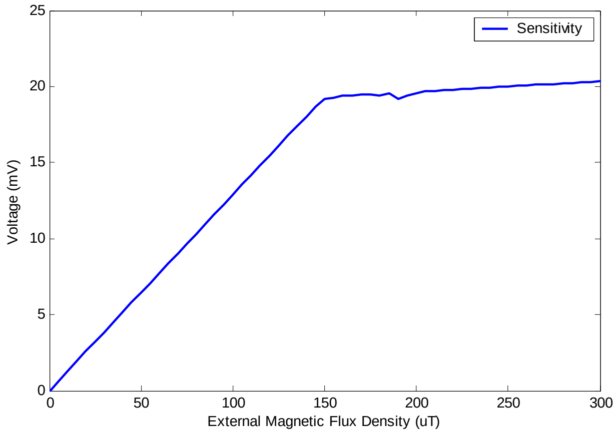

Fig. 22. Optimised Intelligent Sensor's Sensitivity Diagram.

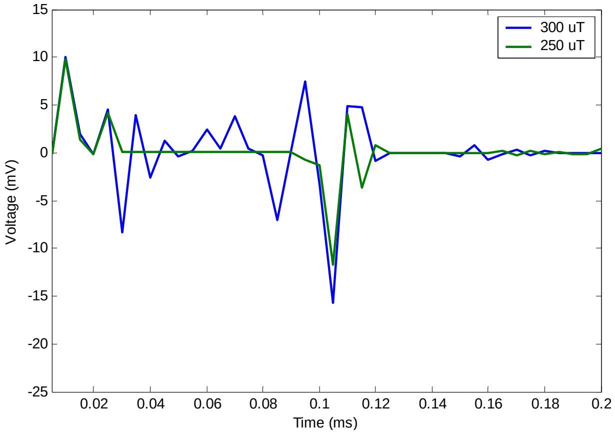

Fig. 23. Output Response for B = 250 and 300 uT.

4. SUMMARY

The design of the basic intelligent sensor and, thereafter, of its optimised version have been explicitly presented. The optimised version of the intelligent sensor is saturated by Iexc of only 60 mA, 4 times less the initial specifications of 250 mA. This leads to a reduction in power consumption by a factor of 16. The intelligent sensor has a guaranteed sensitivity of 100 uV/nT and an output Vpp of 19.45 mV to amply cover the Earth's magnetic field variation. The sensor has a maximum sensitivity of 151 uV/nT.

The results of this study will be used in the development of a full tri-axial intelligent sensor configured by a reconfigurable excitation current source. The tri-axial intelligent sensor can also be built by making an appropriate assembly of three single-axis sensors or by designing a novel compact structure accommodating all xyz directions. Both solutions will be evaluated. In this way, the specifications will be determined for a novel intelligent tri-axial magnetometer for the study of complex space physics events. The system can easily be adapted for both macro-ground-based and micro-space-born applications.

REFERENCES

[1] R. Breckenridge, *Remote Sensing of Earth from Role of Smart Sensors Technical: Role of "Smart Sensors"*, Technical Papers from the AIAA/NASA Conference on Smart Sensors, American Institute of Astronautics & Aeronautics, Vol. 67, 1979.

[2] T. Pham, *Smart Inspection Systems: Techniques and Applications of Intelligent Vision*, Academic Press, 2003.

[3] W. Staszewski et al., *Health Monitoring of Aerospace Structures: Smart Sensor Technologies and Signal Processing*, J. Wiley, 2004.

[4] A. Srinivasan et al., *Smart Structures: Analysis and Design*, Cambridge University Press, 1st Ed., 2000.

[5] V. Seidemann, M. Ohnmacht and S. Buttgenback, *Microcoils and Microrelays-An Optimised Multilayer Fabrication Process*, Sensors and Actuators A, Vol. 83, No.1-3, pp. 124-129, 2000.

[6] T. Meydan, *Application of Amorphous Materials to Sensors*, Journ. Magn. Mater., Vol. 133, pp. 525-532, 1995.

[7] P. Ripka, *Review of Fluxgate Sensors*, Sensors and Actuators A, Vol. 33, pp. 129-141, 1992.

[8] H. P. Thomas, *Direction Responsive System*, U.S. Pat. No. 2,016,977, 1935.

[9] F. M. Neubauer, et al., *The Giotto Magnetic-Field Investigation*, Space Sci. Rev., Vol. 23, p. 250, 1988.

[10] L. R. Alldredge, *Magnetometer*, U.S. Pat. No. 2,856,581, 1951.

[11] F. Primdahl, *The Fluxgate Magnetometer*, J. Phys. E: Sci. Instrum., Vol. 12, pp. 241-253, 1979.

[12] E. O. Schonstedt, *Saturable Measuring Device and Magnetic Core*, U.S. Pat. No. 2,916,696, 1959.

[13] R. Rabinovici and B. Z. Kaplan, *Low Power Portable DC Magnetometer*, IEEE Trans. Magn., Vol. 25, pp. 3411-3413, 1989.

[14] A. Moldovanu, et al., *Functional Study of Fluxgate Sensors With Amorphous Magnetic Materials Core*, Sensors and Actuators A, Vol. 59, pp. 105-108, 1997.

[15] T. Saito, et al., *Magnetometers for Geophysical Use, Part 1. Fluxgate Magnetometer With a 0.5 cm Length Two-Core Sensor*, Science Reports of Tohoku Univ., Sendai, Japan, Ser. 5, Vol. 27, pp. 85-93, 1980.

[16] D. I. Gordon and R. E. Brown, *Recent Advances in Fluxgate Magnetometry*, IEEE Trans. Magn., Vol. 8, pp. 76-82, 1972.

[17] D. B. Clarke, *Demagnetizing Factors of Ringcores*, IEEE Trans. Magn., Vol. 8,

pp. 4440-4444, 1999.
[18] O. V. Nielsen, et al., *Development, Construction and Analysis of the Orsted Fluxgate Magnetometer*, Meas. Sci. Technol., Vol. 6, pp. 1099-115., 1995.
[19] T. Seitz, *Fluxgate Sensor in Planar Microtechnology*, Sensors and Actuators, Vol. A21-A23, pp. 799-802, 1996.
[20] P. Ripka and F. Primdahl, *Tuned Current-Output Fluxgate*, Sensors and Actuators, Vol. A82, pp. 161-166, 2000.
[21] T. M. Liakapolous and C. H. Ahn, *A New Micromachined Fluxgate Sensor Featuring 3-Dimensional Planar Coils*, Sensors and Actuators, Vol.2, 1999.
[22] W. J. Duffin, *Electricity and Magnetism*, McGraw-Hill, 3rd Edition, 1980.
[23] F. Brailsford, *Physical Principles of Magnetism*, Van Nostrand Reinhold, Wokingham, 243, 1966.
[24] K. H. J. Buschow, *Materials Science Reports*, Vol. 1, 1986.
[25] J. D. Kraus, *Electromagnetics: With Applications*, McGraw-Hill, 5th Edition, 1999.
[26] D. Bradley, *Basic Electrical Power and Machines*, Chapman & Hall, 1st Edition, 1994.
[27] F. F. Mazda, *Electronics Engineer's Reference Book*, Butterworth & Co, 6th Edition, 1989.